

Initial magnetic field compression studies using gas-puff Z-pinches and thin liners on COBRA

This article has been downloaded from IOPscience. Please scroll down to see the full text article.

2013 Nucl. Fusion 53 083006

(<http://iopscience.iop.org/0029-5515/53/8/083006>)

View [the table of contents for this issue](#), or go to the [journal homepage](#) for more

Download details:

IP Address: 132.76.61.22

The article was downloaded on 26/08/2013 at 12:33

Please note that [terms and conditions apply](#).

Initial magnetic field compression studies using gas-puff Z-pinches and thin liners on COBRA

P.-A. Gourdain¹, R.J. Concepcion¹, M.T. Evans¹, J.B. Greenly¹,
D.A. Hammer¹, C.L. Hoyt¹, E. Kroupp², B.R. Kusse¹, Y. Maron²,
A.S. Novick¹, S.A. Pikuz¹, N. Qi^{3,4}, G. Rondeau⁴, E. Rosenberg¹,
P.C. Schrafel¹, C.E. Seyler¹ and T.C. Shelkovenko¹

¹ Laboratory of Plasma Studies, Cornell University, Ithaca, NY, USA

² Department of Physics, Weizmann Institute of Science, Rehovot, Israel

³ L3 Pulsed Sciences, San Leandro, CA, USA

⁴ Janx, Piedmont, CA, USA

Received 31 December 2012, accepted for publication 7 June 2013

Published 3 July 2013

Online at stacks.iop.org/NF/53/083006

Abstract

This magnetic compression of cylindrical liners filled with DT gas has promise as an efficient way to achieve fusion burn using pulsed-power machines. However, to avoid rapid cooling of the fuel by transfer of heat to the liner an axial magnetic field is required. This field has to be compressed during the implosion since the thermal insulation is more demanding as the compressed DT plasma becomes hotter and its volume smaller. This compression of the magnetic field is driven both by the imploding liner and plasma. To highlight how this magnetic field compression by the plasma and liner evolves we have separately studied Z-pinch implosions generated by gas puff and liner loads. The masses of the gas puff and liner loads were adjusted to match COBRA's current rise times. Our results have shown that Ne gas-puff implosions are well described by a snowplow model where electrical currents are predominately localized to the outer surface of the imploding plasma and the magnetic field is external to the imploding plasma. Liner implosions are dominated by the plasma ablation process on the inside surface of the liner and the electrical currents and magnetic fields are advected into the inner plasma volume; the sharp radial gradient associated with the snowplow process is not present.

(Some figures may appear in colour only in the online journal)

1. Introduction

Economical inertial confinement fusion may be possible by compressing magnetically a solid cylindrical liner filled with DT fuel [1]. With the advent of modern pulsed-power systems, such concepts have recently received a renewed interest, in particular, Sandia's Magnetized Liner Inertial Fusion (MagLIF) project [2]. Since MagLIF implosion speeds are smaller than the plasma sound speed, the presence of the liner close to the fusion fuel requires an axial magnetic field to insulate the hot compressed plasma from the cold liner. According to [2], a 6 mm diameter liner will be compressed to 0.24 mm. For magnetic insulation to be sufficient, the number of ion Larmor radii from the plasma core to the wall needs to be on the order of 100. As a result, when the plasma temperature reaches 8 keV at the end of the compression, the ion Larmor radius has to be on the order of 1 μm , requiring an axial magnetic field of 10 000 T to ensure sufficient insulation. The plasma cross-section near full compression is 625 times

smaller and reaching 10 000 T from the initial 30 T field requires magnetic field diffusion to be as small as possible.

Such a large magnetic field compression ratio implies efficient and homogenous field compression. If the liner compresses the field faster than the fusion fuel, the axial field on axis will be smaller than at the liner wall. In this case, a magnetic field well will develop on axis (diamagnetism) and confinement will be improved due to inward particle grad- B drift. On the other hand, if the plasma compresses the axial field more efficiently than at the liner interface, then the field on axis will be higher than the field near the liner wall (paramagnetism), and confinement will be degraded due to outward particle drifts. The latter conditions can arise from early plasma compression due to premature plasma ablation on the inner surface of the liner wall. This could initiate early plasma compression and heating, altering the homogeneity of the axial magnetic field across the plasma section. The impact of paramagnetism and diamagnetism on the plasma will be to change not only its local properties but also the overall

dynamics as the implosion develops. Axial magnetic field compression by gas puffs has been reported in the literature, for instance see [3] and more recently [4]. However, this paper shows experimentally and numerically that axial and azimuthal fields arrive on axis at the same time, making it difficult to isolate the compression of the axial magnetic field from the probe or Faraday rotation signals. Picking up an azimuthal field component can be caused by diagnostic misalignment as well as transformation of azimuthal field into axial field by plasma instabilities.

Here we present separate studies of the compression and stability properties of metallic liners and gas-puff Z-pinch on COBRA [5] at Cornell University. This machine is a 1 MA pulsed-power generator with a variable current rise time ranging from 100 to 200 ns. While 1 MA is far from the target current of the MagLIF concept, favourable scaling allows this machine to produce model plasmas for which important dimensionless parameters will be similar to MagLIF plasmas. Four independent plasma parameters can be used to characterize MagLIF plasmas [6]: the ratio of the liner radius to the ion Larmor radius, the ratio of the liner radius to the Coulomb collision mean-free path, the plasma beta and the liner height to radius ratio. In this paper we present initial data on the compression of axial magnetic fields by liners and gas-puff Z-pinch separately. The experimental section describes both experimental setups and diagnostics used to investigate liner and gas-puff implosions. We then discuss the dynamics of both systems with and without external axial magnetic fields. The numerical simulation section presents the PERSEUS code [7] and simulation result of gas puff and liner implosions with and without magnetic fields. Our conclusions will elaborate on the experimental outcome presented herein.

2. Experimental results

2.1. Experimental setup and diagnostics

We used two experimental setups to conduct the initial magnetic field compression studies on COBRA. First we used a supersonic gas-puff valve system with two separate plena that open simultaneously into two nested annular supersonic nozzles. A drawing of the gas-puff valve with the two nested nozzles is shown in figure 1(a). The bore hole traversing the whole valve was used for axial magnetic field measurements using Faraday rotation. This valve was designed and assembled at the Weizmann Institute of Science (WIS) where gas puffs have been extensively studied [8,9]. To avoid damaging the insulator rings inside COBRA from high voltage spikes, the gas puff has to be pre-ionized. Pre-ionization both limits the voltage generated by COBRA at the power feed and enables homogenous and reproducible gas breakdown. The pre-ionizer has a cylindrical copper cathode—mesh anode design. A gas switch is used to trigger the pre-ionizer 10 μ s before the main COBRA current reaches the load. The electrons accelerated in the cathode–anode gap and were not intercepted by the anode mesh ionizing the gas puff. If the gas puff does not trigger correctly, no current flows in the anode cathode gap of the pre-ionizer, in which case an interlock system prevents COBRA from firing. During the initial experimental campaign, the pre-ionizer system was tested. To avoid catastrophic hardware

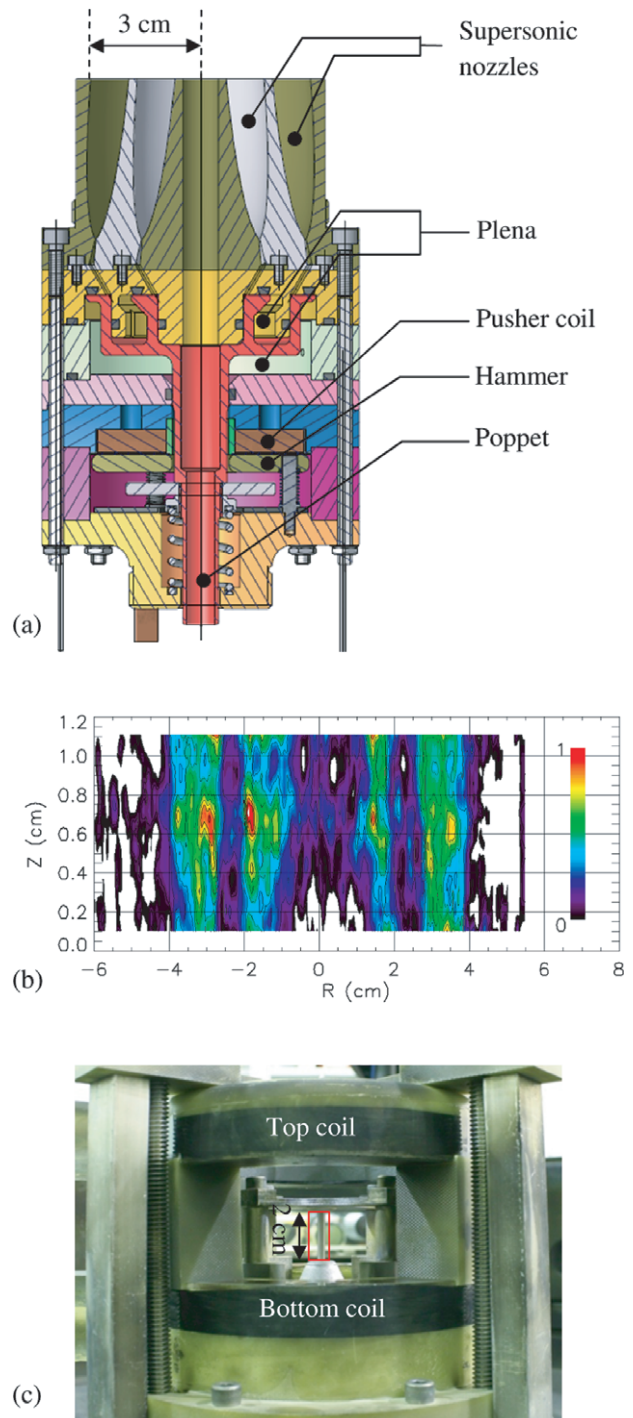


Figure 1. (a) Drawing of the COBRA gas-puff valve with nested nozzle set. The valve has an 8 mm diameter bore hole to facilitate axial magnetic field measurements using B dot probes or Faraday rotation. (b) Planar laser induced fluorescence (PLIF) data for Ne gas at 4 psi. The full scale represents $0.5 \mu\text{g cm}^{-3}$ ($1.5 \times 10^{16} \text{ cm}^{-3}$ ion density). (c) 2 cm tall 3 mm diameter aluminum liner inside the COBRA vacuum chamber (highlighted by the red square). The liner is surrounded by Helmholtz coils that can produce up to 1 T axial field when necessary.

failure by firing the machine into an open circuit, all gas-puff shots presented herein have a wire on axis. This wire protects the machine in case the gas-puff valve fails to open or the pre-ionizer does not fire properly. However, this wire does change

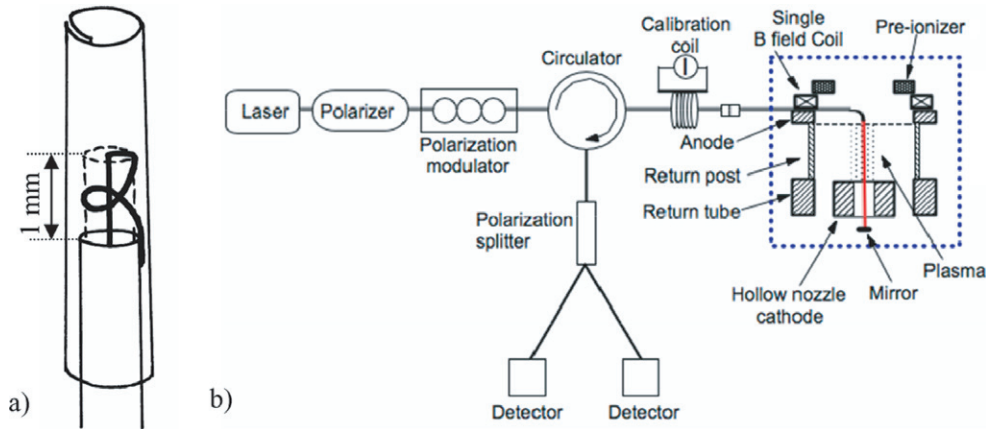


Figure 2. (a) Cartoon of the B_z probe design. Only the conductors are represented. The protecting insulators are left out. (b) Schematics of the fibre FRS and Z-pinch load configuration. The blue boxed area is the Z-pinch region, where the red coloured line is a section of the FRS fibre for sensing the B_z field along the pinch axis.

the gas-puff Z-pinch dynamics and the conclusions regarding magnetic field compression presented in this paper could be different in future experiments, once the wire is removed. Figure 1(b) shows the mass density of Ne gas for the double nozzle system obtained using planar laser induced fluorescence (PLIF). The false colour scale is linear, ranging from the threshold detectable density ($0.01 \mu\text{g cm}^{-3}$) to $0.5 \mu\text{g cm}^{-3}$ (corresponding to $1.5 \times 10^{16} \text{cm}^{-3}$ of ion density) with a measurement error of 15% at the higher densities. Supersonic flow preserves the separation between the two gas shells.

The second experimental setup used a $6 \mu\text{m}$ thick aluminum (Al) liner that was 2 cm tall and 3 mm in diameter, which took advantage of experience gained handling thin foils in several research campaigns studying the plasma dynamics of radial foils [10, 11]. The thin liner was made out of a rectangular, $3 \mu\text{m}$ thick foil that had been rolled twice on a 2.8 mm diameter brass mandrel. The length of the foil is $2\pi \times 3 \text{ mm} \pm 0.2 \text{ mm}$, ensuring that the double wrapped foil forms a liner 3 mm in diameter. This length is critical to minimize overlapping between the two ends of the foil. The double wrap avoids any space between the two seams of the foil, precluding the outer coronal plasma to enter the inner liner volume while providing relatively uniform thickness. The foil height is taller than 2 cm to simplify the positioning of the liner between the anode and cathode. The layered liner stays together under vacuum due to foil tension. The liner, surrounded by the Helmholtz coil pair, is shown in figure 1(c).

Both loads were imploded using 1 MA pulses with 100 ns current rise time. Extreme ultraviolet (XUV) four-frame pinhole cameras were used to record time resolved pictures of plasma self-emission. The typical lower cutoff energy was about 50 eV due to light diffraction from the pinholes (about $100 \mu\text{m}$ in diameter). Laser shadowgraphs were obtained using a pulsed Nd:YAG laser at 532 nm. The laser pulse length was 150 ps, allowing us to take snapshots of the plasma dynamics free of motion blur. The three beam lines are separated in time by 10 ns. The same beam lines gave the areal electron densities from shearing interferometry. Plasma flow velocities (based on ionization front imaging) were measured using a visible light streak camera. Finally, a time integrated pinhole camera was placed inside the vacuum chamber to

record the spatial location of plasma x-ray radiation. Material filters were used to cutoff low energy radiation. We also used miniature B dot probes [12] to measure the change in magnetic field throughout the implosion of gas puffs and liners. The design was altered to measure axial fields. Figure 2(a) shows the geometry of the probe. A foil of copper was used to shield the probe from azimuthal fields. The insulator protecting the probe from the plasma electric fields is not represented. Figure 2(b) shows the Faraday rotation setup. It uses a $\sim 30 \text{ cm}$ single mode SMF-28e fibre with a $>90\%$ reflection gold coated mirror attached at its end. The returning light coming through the circulator (1) allows detection of the returning signal; (2) provides isolation of the laser source from returning light; and (3) doubles the Faraday rotation signal and cancels (or reduces) the polarization shifts induced from mechanical stress. The light then enters a fibre polarization beam splitter (PBS) and is split into two signals with opposite phases. These two anti-phase signals are then detected by two photo-diode detectors. A 1000 turn calibration coil was wound around a section of the fibre and energized by a 3 A, 300 ns, 10 Hz pulser to generate magnetic field for the sensor calibration.

2.2. Gas-puff Z-pinches

For this initial round of experiments, we used Ne gas puffs. The shell axial mass densities were $6 \mu\text{g cm}^{-1}$ for the outer shell and $1.5 \mu\text{g cm}^{-1}$ for the inner shell. A single coil imposed a magnetic field of 0.25 T in the neutral gas before firing COBRA. This field was not homogeneous and had a radial component. Added to this non-ideal field, the presence of the safety wire makes the results presented herein not directly applicable to any MagLIF scaled experiments. However field compression observed during implosions is crucial to report since our conclusions certainly highlight important physical processes taking place during gas-puff implosions. Figure 3 shows the XUV data recorded by four-frame cameras for shot 02591 (without field) and 02601 (with field). Despite the presence of the wire, we can see a noticeable difference in the MRT structure near the implosion time with and without magnetic field. In figure 3(a), we clearly see the presence of instabilities near the axis. Azimuthal correlations, while observed, are not strong. The Ne plasma emission is relatively

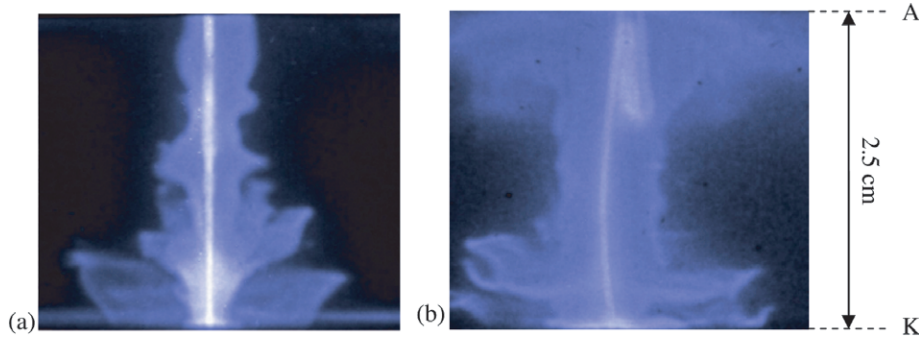


Figure 3. XUV image showing the Ne gas-puff implosion onto the central wire for (a) shot 02591 (no axial field) at 210 ns and (b) shot 02601 (with 0.25 T field) at 210 ns. The exposure time is 2 ns. The anode (A) is at the top, the cathode at the bottom of the picture. The Bdot probe measuring the magnetic field evolution during compression can be seen at the top of the frame, near the pinch axis.

weak in the XUV range compared to the emission from the safety wire. Figure 3(b) shows a slightly different behaviour. While the implosion was not fully reached at the time when the image was taken, the central part of the plasma column is less disturbed by instabilities when the magnetic field has been applied. The minimum value of the external vertical magnetic field B_z necessary to stabilize the MRT instabilities in an imploding annular single gas-puff shell is given by [13]

$$B_z(\text{kG}) = (10 - 30) \frac{I_{\text{max}}(\text{MA})}{R_0(\text{cm})} \quad (1)$$

where R_0 is the maximum shell radius (i.e. before the current pulse starts) and I_{max} is the maximum current of the plasma discharge. Gas puffs were successfully stabilized using this scaling [14]. As a result, the stabilization that seems to take place in figure 3(b) could be attributable to the external field despite the fact that this field is neither homogeneous nor purely axial. While more experimental data are required to confirm this effect, the observed stabilization seems to be consistent with the empirical scaling of equation (1).

Figure 3(b) also shows the location of the miniature Bdot probe that recorded the change in magnetic field during the gas-puff implosion. The data measured by this probe are presented in figure 4(a) together with the plasma current and the x-ray sensitive photo-conductive detector (PCD) signals that indicate when the plasma reaches stagnation. The corresponding magnetic field, obtained from the time integrated signal of the probe, is also plotted. The implosion occurs 175 ns into the shot according to the radiation signal on the PCDs. Only then the Bdot probe records a substantial change in magnetic field. The probe was oriented to pick up axial field changes only. Two shots were made with a B_z dot probe, measuring dB/dt , in gas puffs with applied (axial) B_z field, and one shot with a B_z dot probe and zero applied field. All three showed probe signals beginning late in the current pulse near the implosion (x-ray signal rise) time, and they were of similar amplitudes. The initial sign of one of the B_z dot probe signals was positive, consistent with an increase of the applied B_z field. In the other B_z dot probe signal (the one shown in figure 4(a)), the applied field began by going negative, but reversed after ~ 10 ns and its main peak was positive. Figure 5 shows a comparison of the signals measured by two different Bdot probes built on the same design with applied axial field (shot #02600 as in figure 4) and without the applied axial field (shot #02602). As

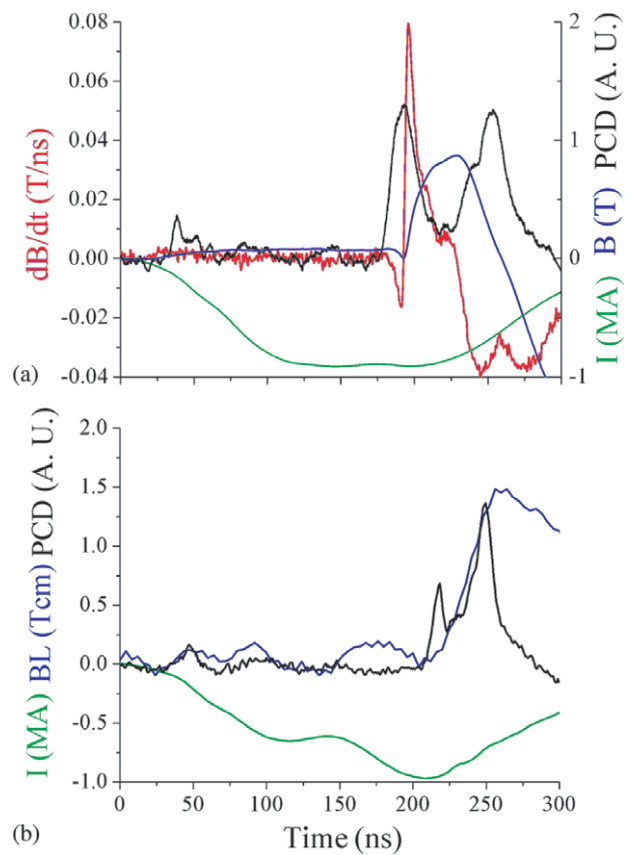


Figure 4. (a) Time evolution of the Bdot signal (red), the magnetic field (blue), the plasma current (green) and the PCD signal (black) for shot 02600. (b) Time evolution of the Faraday rotation signal (blue), the PCD signal (black), and the plasma current (green) for shot 02606.

one can clearly see, the probe picks up a change in magnetic field at implosion. At the moment we do not know if the pickup is due to probe misalignment or plasma instabilities which force some of the plasma current to flow azimuthally instead of axially. As a result, it is not possible to affirm that the signal recorded by the probe represents axial field compression. However it does record the time when the total (axial, radial and azimuthal) field reaches the axis. This clearly happens near maximum implosion. Keeping in mind that the azimuthal field could be responsible for a large portion of the Bdot signal we recorded a magnetic field of 1 T near the axis

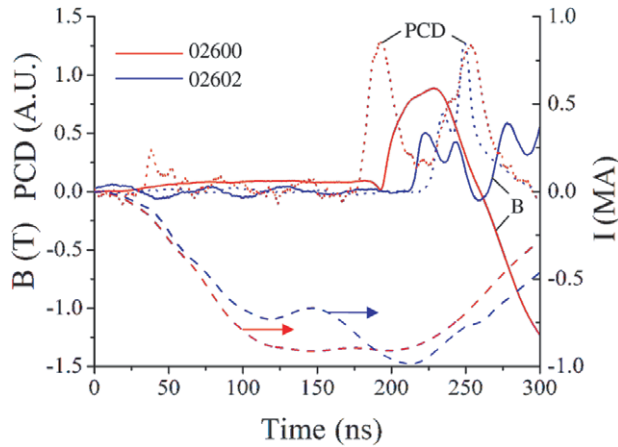


Figure 5. Time evolution of the measured magnetic field, the plasma current and the PCD signal for shot 02600 (red) and 02602 (blue).

at full implosion. To corroborate this measurement, we turned to Faraday rotation using an optical fibre as the propagation medium. The fibre is placed along the axis of the gas puff. While the fibre is not sensitive to electrostatic pick up from the plasma, it is sensitive to physical alignment, three-dimensional magnetic field from plasma instabilities and damage from the implosion shock wave. However, this diagnostic, based on completely different physical principles, corroborates the $B\dot{\theta}$ probe measurements. Figure 4(b) shows that 0.64 T magnetic field was recorded at full implosion, consistent in timing with $B\dot{\theta}$ probe measurements and happening when the plasma reaches the axis.

This gas-puff implosion experimental campaign demonstrated that $B\dot{\theta}$ and fibre-based Faraday rotation measurements show that magnetic field is present near the pinch axis only at full implosion. While both systems were set up to measure axial magnetic fields, these two independent measurements did measure a portion of the total field on axis rather than the axial field alone.

2.3. Liner implosions

We now turn to liner compression studies. To exacerbate plasma instabilities like kink and MRT instabilities we chose to study tall liners. Figure 6 shows the time evolution of the liner implosion recorded by a streak camera in visible light. Figure 6(a) shows the two-dimensional spatial data recorded by the camera. The camera streaks the dotted red line across the screen of an intensified CCD camera. The left-hand side of the streak camera records the time evolution of the plasma along the diameter of the liner, the right-hand side records the time evolution of the plasma along the height of the liner. A laser fiducial, used to synchronize the data with the machine current, is indicated on the image and should not be mistaken for plasma self-emission. The left-hand side of figures 6(b) and (c) show the coronal plasma along the diameter of the liner. This plasma is mostly stationary during the first half of the pulse. After implosion, the plasma expands outward. There is no strong indication that the liner imploded from visible imaging, possibly due to the accumulation of neutral gas around the pinched liner. This gas emits visible light which shields the actual dynamics of the liner. The compressed

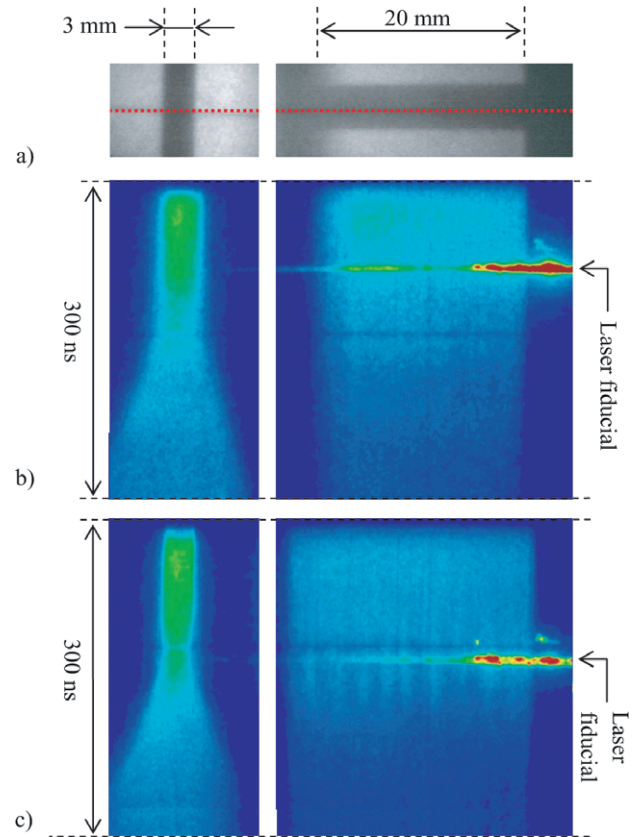


Figure 6. Visible streak camera data. (a) Black and white image of the liner with its axis vertical (left) and with its axis horizontal (right). The time evolution of the plasma was recorded along the dotted red line. The time evolution across the red dotted line for (b) a short current pulse (100 ns current rise time: shot #02587) and (c) a long current pulse (200 ns rise time: shot #02574) in false colour to enhance the contrast of the black and white images.

liner self-emission is also in the vacuum UV and soft x-ray spectra, which are not captured by this camera. The right-hand sides of figures 6(b) and (c) show the data recorded along the liner height and do not exhibit any visible non-uniform electrical breakdown. Pulses with slow rise times do show non-uniform breakdown around the liner waist. The right-hand side of figure 6(c) shows that the edges of the liner breakdown first (concave shape of the light signal). The ionization wave reaches the side facing the streak camera in less than 10 ns. The right-hand side of figure 6(c) shows that the liner is uniformly illuminated along its height at this time. While we did not observe noticeable $m = 0$ instabilities in the 100 ns rise-time pulse of figure 6(b), they clearly appear on figure 6(c) (after the time marked by the laser fiducial) for the 200 ns rise-time pulses.

However, plasma instabilities do exist even for fast rising current pulses as shown in figure 7. They simply do not appear in the visible light signal. Starting from the cylindrical liner of figure 7(a), laser shadowgraphy reveals that plasma instabilities plague the fully imploded liner as shown in figure 7(b). The plasma ‘shadow’ is caused by electron density gradients that refract laser light out of the optical system when the line average density is above 10^{20} cm^{-3} for this particular setup. When comparing these data to plasma radiation above 1.2 keV in energy recorded by an x-ray pinhole camera, shown

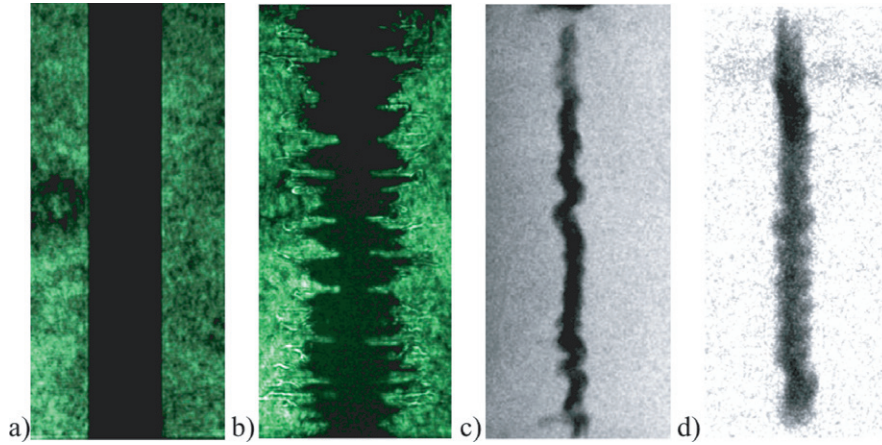


Figure 7. Laser shadowgraph of the liner (a) before the shot and (b) when fully imploded at $t = 150$ ns; and (c) time integrated x-ray pinhole camera image with lower energy cutoff at 1200 eV for shot #02575. (d) Time integrated x-ray pinhole camera with lower energy cutoff at 1200 eV with axial field for shot #02614. The total height of the liner is 2 cm and its diameter is 3 mm.

in figure 7(c), it is clear that the liner had fully imploded. The necks visible in figure 7(b) are instabilities which started as MRTs and turned into $m = 0$ instabilities. The kink instability is also visible on figure 7(c). While it is difficult to identify the footprint of the central plasma column of figure 7(c) in the laser shadowgraph, the diameter of the plasma column is similar in size to the neck diameters visible in figure 7(b).

As discussed earlier, a 1 T axial field generated by a pair of Helmholtz coils was applied in the next series of shots. The magnetic field had a rise time of 120 μ s. However, a large volume of the magnet bore was occupied by brass electrodes. The induced currents inside the hardware did degrade the homogeneity of the axial field and, while the maximum field strength was about 1 T, the actual field distribution was not purely axial at the liner location. However, the impact of the field is clearly visible since it seems that the kink instability has been partially suppressed, as seen on figure 7(d). The time evolution of the magnetic field was measured by a $B_{\dot{\theta}}$ probe with a design similar to the one used in the gas-puff Z-pinch experiments. Two shots were made with a probe inside a liner with an applied (axial) B_z field, and one shot with a B_{θ} probe, also with applied B_z . All three showed signals starting at similar times, early in the pulse and long before implosion of the liner. Figure 8 shows the time evolution of the magnetic field recorded by the axial $B_{\dot{\theta}}$ probe. The field magnitude measured by the B_{θ} probe was 3–5 times larger than the fields inferred from the B_z probe signals. The two B_z signals were both initially positive, in the direction of an increase of the applied field. After the first peak all three signals reversed sign, but the B_{θ} signal and one of the B_z signals came back quickly to positive while the other B_z signal remained negative. This irreproducibility in sign and magnitude may be an indication of departure from symmetry of the plasma currents flowing in proximity to the probe surface. It is known that probes placed within 2 mm of the axis of wire array Z-pinches drastically perturb the current channel formed near the axis by ablated plasma. No Faraday rotation measurements were done for this setup due to the large diameter of the optical fibre. However we can affirm that magnetic field is present near the axis 30 to 50 ns into the current pulse from the probe signals.

In summary, the appearance of B_{θ} near the axis very early in the pulse is definitely shown by these data, and is

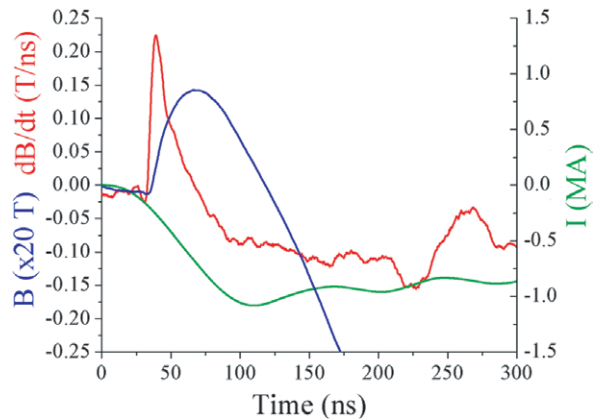


Figure 8. Time evolution of the $B_{\dot{\theta}}$ signal (red), the magnetic field (blue) and the plasma current (green) for shot 02609.

consistent with advection by ablated plasma from the inside of the liner as the simulations will show in the next section. The B_z probe signals are consistent in character with a possible early compression of the applied B_z field, but this cannot be definitely inferred from these initial data because of the sensitivity of the probes to the larger B_{θ} field arriving at the same time.

3. Numerical simulations

3.1. The PERSEUS code

For this paper, numerical simulations were carried out with the three-dimensional PERSEUS [7] code which solves the two-fluid model in the generalized Ohm's law (GOL) formulation. The additional physics currently in the model that goes beyond standard MHD includes electron inertia and the Hall effect. The form of the GOL we use is

$$E = -u \times B + \eta J + \frac{1}{en_e} [J \times B - \nabla \cdot (p_e I)] + \frac{m_e}{n_e e^2} \left[\frac{\partial J}{\partial t} + \nabla \cdot \left(u J + J u - \frac{1}{en_e} J J \right) \right]. \quad (2)$$

The electron inertial physics enables a consistent treatment of the low density (or vacuum) regions, obviating the need for

an unphysical vacuum resistivity. The fully electromagnetic implementation of Maxwell's equations and the Hall term enables a consistent calculation of all the electric field components and enables the application of general boundary conditions. The code uses an implicit-explicit monotone upwind scheme for conservation laws (MUSCL) scheme [15]. The equations are discretized using a finite volume approach based on the freezing speed method which uses the Lax–Friedrichs flux modified by the appropriate use of the eigenvalues of the flux Jacobian. This method eliminates the need for an expensive Riemann solver, and the source terms on the right-hand side of the equations are easily accommodated. The method is approximately second order in space through the use of a flux-limited MUSCL scheme. The details of the algorithm can be found in the thesis by Martin [16].

The code has been tested and benchmarked in multiple ways. We have verified that PERSEUS reproduces known MHD and hydrodynamic shock solutions in the appropriate limits. We have also shown that low-frequency dispersive behaviour due to the Hall effect is correctly computed and that high frequencies are implicitly suppressed by the numerical algorithm to inhibit numerical instability for large time steps. A comparison of PERSEUS to the MHD code GORGON [17] for wire array implosions shows similar results, but reveals differences that are attributable to the physical differences in the plasma models. The code easily handles 9 orders of magnitude in density variation in single precision and more in double precision. Since the equations are solved in conservation form using a shock capturing scheme the algorithm is particularly suitable to simulate gas-puff Z-pinch and liner implosions. The electron pressure term was turned-off in both simulations. While the Hall term is often considered negligible in high energy density plasmas, it was shown recently that Hall physics can impact the plasma dynamics even when the ion inertial length is small compared to the scale length of the system [18]. As a result, we believe that Hall physics should be included in the numerical simulations of gas-puff Z-pinch and thin liner implosions.

3.2. Gas-puff Z-pinch

The Ne gas-puff Z-pinch was modelled using a three-dimensional domain of 11 cm in both width and length and 2.5 cm in height. We used grid resolution of $344 \mu\text{m}$ on all directions, populating the whole volume with a little bit less than 8 million cells. The ionization number was kept constant (i.e. $Z = 3$) throughout the simulation. The volume height corresponds to the experimental distance between the anode and cathode used in the experiments presented in the previous section. We did not include a safety wire in our simulations. The initial plasma ion density corresponds to the neutral density obtained from the PLIF data. We modelled the gas-puff spread using a mass conserving axisymmetric Gaussian distribution profile. The profile was peaked at the midpoint radius between the inner and outer walls of each nozzle. Figure 9 shows results of the PERSEUS simulation with and without axial field. Only three quarters of the plasma volume is presented so the full height of the pinch is visible on the left plane of the cut volume. On the right cut, the axial magnetic field was plotted instead of the plasma density. Both

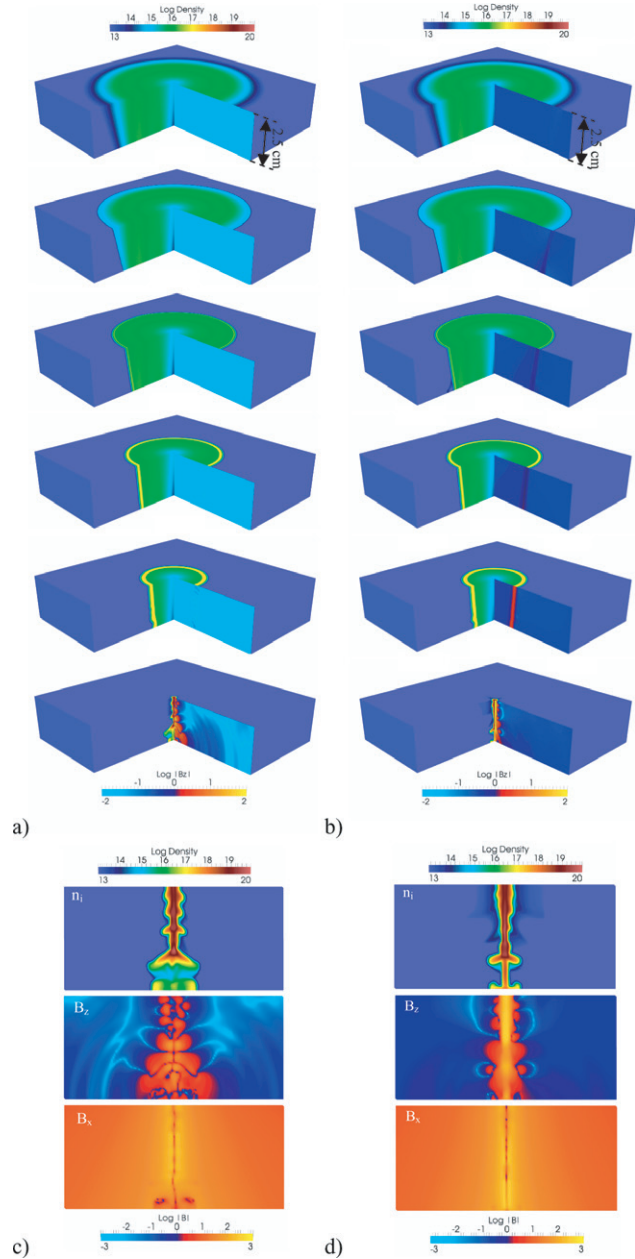


Figure 9. Time evolution of the gas-puff Z-pinch implosion with (a) no initial external axial field and with (b) a 0.25 T initial axial field. The plasma ion density (in cm^{-3}) is plotted for three quarters of the plasma volume. The colour scale corresponds to log ion density. Densities above 10^{20}cm^{-3} and below 10^{13}cm^{-3} were clipped at the maximum and minimum values, respectively. The plane on the right side of each picture gives the axial field strength (in T) also on a log scale. Fields above 10^2T and below 10^{-2}T were clipped at the maximum and minimum values, respectively. The anode plane is at the top and the cathode plane is at the bottom. The time slices are separated by 33.33 ns starting at $t = 6.66 \text{ns}$. Plasma ion density, axial and azimuthal magnetic fields at stagnation are plotted with (c) no initial external axial field and with (d) a 0.25 T initial axial field. The height of both pinches is 2.5 cm. The ion density and magnetic field strength are on the \log_{10} scale.

density and field colour scales are \log_{10} scales instead of linear scales, allowing the ion and field distributions to be plotted over many orders of magnitude. Values above or below the field and density scale limits were clipped. As a result, while

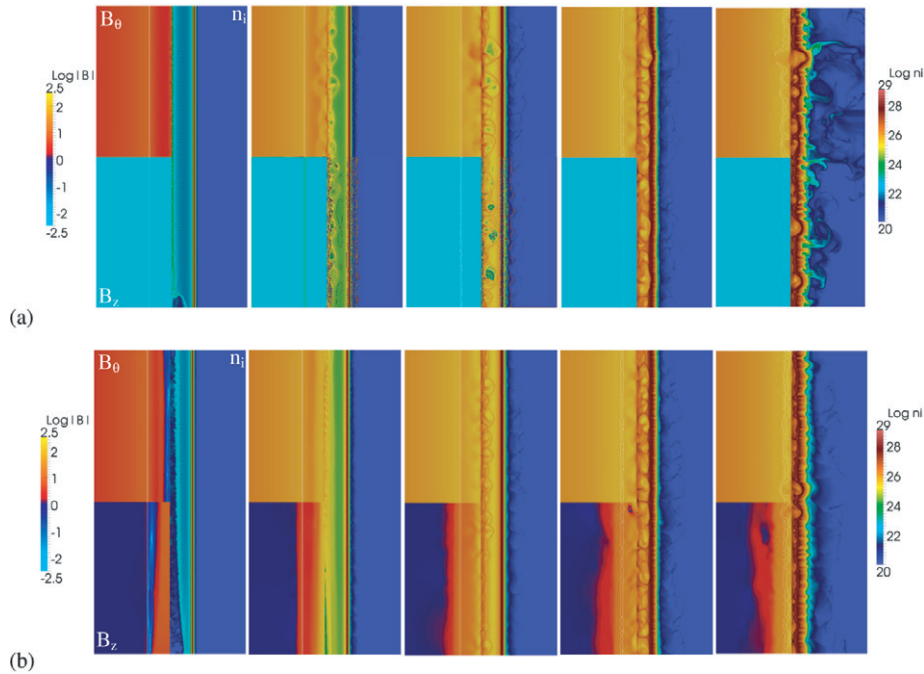


Figure 10. Time evolution of the liner implosion (a) with no axial field and (b) with 1 T axial field in two dimensions using a cylindrical coordinate system. For each time slice, the axial field, the azimuthal field and the plasma ion density are plotted on a \log_{10} scale. Densities above 10^{29} m^{-3} and below 10^{20} m^{-3} were clipped at the maximum and minimum values, respectively. Fields above $10^{2.5} \text{ T}$ and below $10^{-2.5} \text{ T}$ were also clipped at the maximum and minimum values, respectively. The time slices are separated by 40 ns starting at $t = 20 \text{ ns}$. The height of the computational domain is 2 cm. The anode is at the top and the cathode is at the bottom. The white lines on the left panels are iso-density lines for ion density equal to $10^{27.5}$.

there is no field on the first time slice in figure 9(a), the colour scale does not represent the absence of field at this time.

When no field is present, figure 9(a) shows a gas implosion with moderate MRT instabilities compared to wire loads in COBRA. The instability amplitude is on the order of 20% of the pinch height. The time evolution in figure 9(a) shows that the plasma is snowplowed by the magnetic field all the way to the axis. At stagnation, these instabilities generate an axial magnetic field on the order of 56 T while the total azimuthal field is 220 T (figure 9(c)). Figure 9(b) shows the plasma dynamics is similar when an axial field is present except near stagnation where the amplitude and spatial frequency of the MRT are reduced. Axial field compression is large in the simulation. Starting from 0.25 T, the axial field reaches 380 T on axis at stagnation (figure 9(d)). The coarse resolution of the computational domain and the relatively simple resistivity model (i.e. simplified Spitzer+Lee/More/Desjarlais [7]) can overestimate the actual axial magnetic field compression compared to experimental measurements. Thus, we cannot do a one-to-one comparison between experimental and computational results. However, both simulations and experiments agree on one major point: no sizable axial (or azimuthal) field increase is observed on axis until the outer, current-carrying layer of the plasma reaches this location.

3.3. Liner implosions

The liner implosions were modelled using a two-dimensional domain with cylindrical coordinates. The domain is 6 mm in radius and 20 mm in height. We used grid resolution of $30 \mu\text{m}$

on all directions, populating the whole domain with a little less than 113 000 cells. The ionization number was kept constant (i.e. $Z = 3$) throughout the computation. The aluminum liner is $6 \mu\text{m}$ thick and 1.5 mm in radius. Figure 10(a) shows the simulation of liner implosion with no axial field. On the left-hand side the axial (B_z) and azimuthal (B_θ) field are plotted on the \log_{10} scale. Values above or below the scale limits were clipped. Since the axisymmetric simulation was started with no axial field, there is no axial field present in the whole simulation. This simulation shows that plasma ablation of the inner surface of the liner occurs early. At 20 ns into the simulation, the ablated plasma has reached the axis. Throughout the simulation, the plasma ablated on the inner surface of the liner is advected towards the axis and drags azimuthal magnetic field with it. The azimuthal field in close proximity to the axis is on the same order as the azimuthal field in the outer volume of the liner. As was seen experimentally (i.e. figure 8), the inner volume of the liner fills with magnetic fields at early times ($t < 20 \text{ ns}$), indicating that the field penetration and plasma ablation are strictly coupled together.

When an axial field of 1 T is added to the simulation, the overall plasma dynamics is similar. Subtle differences highlight the effect of the axial field on the ablated plasma inside the liner. Due to axial field compression, the ablated plasma from the inner surface of the liner reaches the axis later. The growth of the plasma instabilities near the axis is also reduced. At later times, the amplitude of the instabilities in the imploding liner is also reduced. This is consistent with the stabilizing effect of the axial field. As one can infer from basic MHD arguments, axial field compression is clearly

occurring in the simulation. However, the field compression reaches a maximum value near current peak, the field strength staying below this value at subsequent times; there is no significant increase in axial field after 150 ns. Most of the field compression is done by the ablated plasma rather than the liner itself. With or without axial field, there is a noticeable amount of trailing mass surrounding the imploding liner. This was also seen experimentally (i.e. figures 6 and 7(b)). While 2D computations do not allow us to elaborate on the kink stabilization observed in the experiment when a 1 T axial field is present, the necks visible experimentally appear in the numerical simulations. The amplitude of plasma instabilities in the trailing mass is reduced compared to the case where no field is present.

4. Conclusions

In this paper, we have focused our research on the basic mechanisms involved in axial field compression in high energy density plasmas by studying separately Ne gas-puff *Z*-pinches and imploding Al liners. While Ne and Al have similar atomic numbers, our work highlighted how differently the dynamics proceeds when the mass is concentrated in a thin liner versus the broad radial distribution of mass in a gas puff.

On one hand, gas-puff *Z*-pinches tend to carry currents in a surface layer, resulting in snowplow-like implosions. Experimental measurements showed that there is little magnetic field change inside the gas volume until the outer, cylindrical current shell reaches the $B\dot{\text{dot}}$ probes or the optical fibre. While axial field compression could not be measured due to parasitic pickup of the azimuthal field, the absence of field during most of the discharge in the central volume surrounded by the imploding current channel has been verified. Numerical simulations agree qualitatively with the experimental measurements. Since most of the plasma energy comes from electromagnetic energy, the absence of currents in the central region of the gas puff indicates that the plasma dynamics there is relatively quiescent compared to the plasma dynamics where currents flow.

On the other hand, the dynamics of imploding thin liners is dominated by the plasma ablation, which carries a substantial portion of the axial and azimuthal magnetic fields towards the axis. Well before the densest part of the liner starts to implode, a sizeable amount of plasma is present on axis. Numerical simulations find similar timing with experimental measurements for the arrival of plasma/field on axis. As previously discussed, the compression of axial magnetic field could not be evaluated due to parasitic pickup of the azimuthal field. Numerical simulations indicate that most of the field compression is due to plasma ablation rather than due to liner implosion. While larger fields can delay the actual compression, the field diffusion across the plasma may become an issue and the resistivity models should be improved so reasonable conclusions can be drawn from numerical simulations.

Overall, this research shows that reliable axial field compression measurements are difficult to obtain since axial and azimuthal fields are tightly coupled inside the plasma. As a result, the overwhelming strength of the azimuthal field makes the measurements of the axial field a challenge. Being able

Table 1. Possible plasma properties for MagLIF-like implosion on COBRA.

	Radius (mm)	Length (mm)	Density (cm ⁻³)	Temperature (eV)	Total magnetic field (kG)
Initiation	1.50	3	5.75×10^{17}	9.3	2.32
Implosion	0.12	3	4.47×10^{19}	32.8	54

Table 2. Dimensionless plasma parameters for MagLIF-like implosion on COBRA and the planned MagLIF parameters from [6].

	$\frac{a}{\rho_i}$	$\frac{a}{\lambda}$	β	$\frac{L}{a}$
Initiation COBRA	0.5	333	80.5	2
Implosion COBRA	0.5	166	40	25
Initiation MagLIF	22.7	333	80.5	2
Implosion MagLIF	76.4	7.5	4.57	50

to measure the weaker, external axial field (at least an order of magnitude smaller) requires a very careful design of $B\dot{\text{dot}}$ probes and Faraday rotation measurement hardware. However, this research does demonstrate that gas-puff *Z*-pinches appear to obey snowplow physics while liners are dominated by ablation physics. These preliminary experiments seem to make COBRA an excellent platform to study MagLIF ‘mock-up’ plasmas. Since it is not possible to meet all the compression and heating criteria of MagLIF, we have to relax at least one parameter. The particular physics associated with this parameter would not be investigated. For instance, if we desire to study magnetic field compression, one may argue that the plasma needs to be hot enough to allow magnetic field compression as it implodes, yet the field may not have to confine ions beyond tens of eV, relaxing the ratio of the plasma radius to the Larmor radius. Based on the results presented in this paper, table 1 shows the plasma properties that could be obtained using COBRA’s current pulse with a 6 μm thick liner.

The plasma properties given in table 1 correspond to the dimensionless parameters given in table 2.

Here a is the liner radius, ρ_i is the ion Larmor radius, λ is the Coulomb collision mean-free path, β is the ratio of kinetic to magnetic pressure and L is the liner height. This table shows that using MagLIF initial parameters but for the Larmor parameter given in the first column (and which we kept constant), then COBRA’s implosion will have the same dimensionless parameters as MagLIF half way through the compression ramp.

Acknowledgments

This research was supported by the Stewardship Sciences Academic Alliances program of the National Nuclear Security Administration under NNSA/DOE Grant Cooperative Agreements number DE-FC52-06NA 00057, DE-NA 0001836 and NSF Grant No PHY-1102471. The authors would like to thank H. Wilhelm and T. Blanchard for their technical support.

References

- [1] Goldberg S.M., Liberman M.A. and Velikovitch A.L. 1990 *Plasma Phys. Control. Fusion*. **32** 319

- [2] Slutz S.A., Herrmann M.C., Vesey R.A., Sefkow A.B., Sinars D.B., Rovang D.C., Peterson K.J. and Cuneo M.E. 2010 *Phys. Plasmas* **17** 056303
- [3] Felber F.S., Wessel F.J., Wild N.C., Rahman H.U., Fisher A., Fowler C.M., Liberman M.A. and Velikovich A.L. 1988 *J. Appl. Phys.* **64** 3831
- [4] Sorokin S.A. 2010 *IEEE Trans. Plasma Sci.* **38** 1723
- [5] Greenly J.B., Douglass J.D., Hammer D.A., Kusse B.R., Glidden S.C. and Sanders H.D. 2008 *Rev. Sci. Instrum.* **79** 073501
- [6] Ryutov D.D., Cuneo M.E., Herrmann M.C., Sinars D.B. and Slutz S.A. 2012 *Phys. Plasmas* **19** 062706
- [7] Seyler C.E. and Martin M.R. 2011 *Phys. Plasmas* **18** 012703
- [8] Kroupp E., Osin D., Starobinets A., Fisher V.I., Bernshtam V., Maron Y., Uschmann I., Forster E., Fisher A. and Deeney C. 2007 *Phys. Rev. Lett.* **98** 115001
- [9] Kroupp E. *et al* 2011 *Phys. Rev. Lett.* **107** 105001
- [10] Gourdain P.A., Blesener I.C., Greenly J.B., Hammer D.A., Knapp P.F., Kusse B.R. and Schrafel P.C. 2010 *Phys. Plasmas* **17** 012706
- [11] Gourdain P.-A., Blesener I.C., Greenly J.B., Hammer D.A., Knapp P.F., Kusse B.R., Pikuz S.A. and Shelkovenko T.C. 2010 *Plasma Phys. Control. Fusion* **52** 055015
- [12] Greenly J.B., Martin M.R., Blesener I.C., Chalenski D.A., Knapp P.F. and McBride R.D. 2008 *7th Int. Conf. on Dense Z-Pinches (Alexandria, Virginia, USA); AIP Conf. Proc.* **1088** 53
- [13] Bud'ko A.B. *et al* 1989 *Phys. Fluids* **B1** 598
- [14] Shishlov A.V. *et al* 2006 *Laser Phys.* **16** 183
- [15] van Leer B. 1979 *J. Comput. Phys.* **32** 101
- [16] Martin M. 2010 Generalized Ohm's law at the plasma–vacuum interface *PhD Dissertation* Cornell University
- [17] Chittenden J P *et al* 2001 *Phys. Plasmas* **8** 2305
- [18] Gourdain P.-A. and Seyler C.E. 2013 *Phys. Rev. Lett.* **110** 015002